Aerodynamics of Highway Sign Structures: From Laboratory Tests and Field Monitoring to Structural Design Guidelines

Michael Heisel[1]; Carly Daugherty[2]; Nicole Finley[3]; Lauren Linderman, A.M.ASCE[4]; Dominik Schillinger[5]; Catherine E. French, Dist.M.ASCE[6]; and Michele Guala, Ph.D.[7]

Abstract: Field- and model-scale experiments were conducted to quantitatively assess the effects of wind loading on Rural Intersection Conflict Warning System (RICWS) highway sign structures. A field-scale RICWS was instrumented with acceleration and linear displacement sensors to monitor unsteady loads, dynamics, and displacement of the sign under various wind events classified by cup and vane wind velocity measurements. To complement the field-scale results, tests on a 1:18-scale model were conducted under controlled laboratory conditions in the St. Anthony Falls Laboratory towing tank and wind tunnel facilities. Aerodynamic effects on the sign structure were identified through analysis of the mean and oscillating drag and lift forces. Vortices periodically shed by the structure induced forces at a frequency governed by the Strouhal number. The shedding frequency overlapped with the estimated natural frequency during strong wind events, leading to possible resonance. Amplified oscillations were additionally observed when the wind direction was parallel to the structure, possibly due to an aeroelastic instability. The findings highlight the relevance of aerodynamic effects on roadside signs or similar complex planar geometries under unsteady wind loading. **DOI: [10.1061/(ASCE)ST.1943-541X.0002798](https://doi.org/10.1061/(ASCE)ST.1943-541X.0002798).** © *2020 American Society of Civil Engineers.*

Introduction

Highway signs are inherently exposed to significant environmental wind-loading events such as natural wind gusts, which can cause failures when fatigue-loading and aerodynamic effects are not considered in the design of the structure (Chen et al. 2005; Chang et al. 2009; Solari 2017; Kareem et al. 2019). Roadside structures are critical to the safety of travelers and the uninterrupted flow of traffic, making the reliability of the signs a serious priority (Hong et al. 2014). As a result, the AASHTO Specification for Structural Supports for Highway Signs, Luminaires, and Traffic Signals (2017) addresses fatigue design under wind loading for overhead sign and signal structures and high mast light towers.

One recognized contribution to the instability of sign supports is vortex shedding caused by wind loading (Hosch and Fouad 2009; Connor et al. 2012; Sherman and Connor 2019). A solid structure immersed in a fluid flow generates vortices in its wake. These wake vortices, known as Kármán vortex streets, are ubiquitous in aeronautical, urban, and geophysical environments (Roshko 1954; Berger and Wille 1972). The vortices form along the side of the structure and detach in the wake in a periodic manner, leading to unsteady forces and displacements known as vortex-induced vibrations imposed on the structure by the flow (Norberg 2001; Williamson and Govardhan 2004; Kareem and Wu 2013; Wu and Kareem 2013; Simiu and Yeo 2019). The frequency of the periodic vortex shedding is described by the dimensionless Strouhal number, which depends on the flow speed and the structure geometry (Roshko 1954; Lienhard 1966; Levi 1983; Bokaian and Geoola 1984). Studies have been conducted to understand and model the vortex shedding of flat plates, which are representative of many roadway signs exposed to wind loads (Yang et al. 2012; Rai 2013). In particular, examination of vortex shedding of yawed (not perpendicular to the mean flow) flat plates has revealed the asymmetric behavior of vortices when the flow is not normal to the face of the plate (Lam and Wei 2010). These findings are especially relevant for road signs because outdoor structures are exposed to wind loading from all directions and must be designed bearing this in mind.

Fatigue design for roadside signs due to wind loading, particularly vortex shedding, is currently not addressed due to their relatively smaller scale (AASHTO 2017; Garlich and Thorkildsen 2005). However, among the many modifications and attachments complying with updated regulations, the usage of large, electronic roadside signs mounted on supports designed for lighter sign structures is increasing and deserves further study. These structures may be susceptible to instability of the supports and fatigue under wind loading. Inclusion of modern electronic signage often increases the mass and thickness of the sign. These increases, along with construction,

[1]Ph.D. Candidate, St. Anthony Falls Laboratory, Dept. of Civil, Environmental, and Geo Engineering, Univ. of Minnesota, 500 Pillsbury Dr. SE, Minneapolis, MN 55455 (corresponding author). ORCID: https://orcid.org/0000-0002-4200-5550. Email: heise070@umn.edu

[2]Undergraduate Student, Dept. of Civil, Environmental, and Geo Engineering, Univ. of Minnesota, 500 Pillsbury Dr. SE, Minneapolis, MN 55455. ORCID: https://orcid.org/0000-0003-2076-8917

[3]Master's Student, Dept. of Civil, Environmental, and Geo Engineering, Univ. of Minnesota, 500 Pillsbury Dr. SE, Minneapolis, MN 55455.

[4]Associate Professor, Dept. of Civil, Environmental, and Geo Engineering, Univ. of Minnesota, 500 Pillsbury Dr. SE, Minneapolis, MN 55455.

[5]Associate Professor, Dept. of Civil, Environmental, and Geo Engineering, Univ. of Minnesota, 500 Pillsbury Dr. SE, Minneapolis, MN 55455.

[6]Professor, Dept. of Civil Engineering, Univ. of Minnesota, Minneapolis, MN 55455.

[7]Associate Professor, St. Anthony Falls Laboratory, Dept. of Civil, Environmental, and Geo Engineering, Univ. of Minnesota, 500 Pillsbury Dr. SE, Minneapolis, MN 55455.
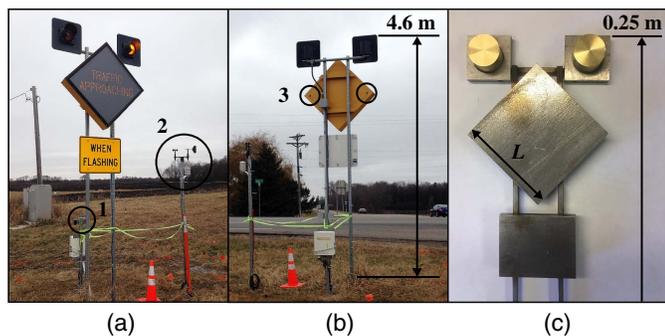
Fig. 1. Setup of the instrumented RICWS highway sign: (a) front view showing (1) the cup and vane anemometer and (2) string potentiometer; (b) rear view showing (3) the accelerometers; and (c) model sign structure scaled 1:18 for laboratory testing, including the two top light plates, diamond-shaped center panel with side length L, and lower rectangular plate.

geometry, and site variability, can alter the critical stability conditions and vibration response of signs (Williamson and Govardhan 2004; Amy et al. 2009). The structural support of the sign must therefore be reevaluated following changes to the sign design.

One example of a sign recently updated with electronic components is the Rural Intersection Conflict Warning System (RICWS), which was first introduced by the Minnesota DOT (MnDOT) in Spring 2013 (MnDOT 2014). The purpose of the RICWS sign is to communicate live information to drivers about oncoming traffic. Specifically, drivers on the minor road of a rural intersection are informed of whether vehicles are approaching on the major roadway. By providing this information, MnDOT hopes to reduce the number and severity of collisions at such intersections (MnDOT 2014). To display this information, the RICWS sign has an electronic diamond face with the message "Traffic Approaching" as well as two lights above the diamond face which flash when there is traffic on the main road [Fig. 1(a)]. The electronic sign is six times heavier than the traditional diamond face. As a result, the response of updated RICWS signs to wind loading is different than previous versions of the sign, and structural failures have occurred with the new RICWS sign structure (MnDOT 2016). An additional concern is the requirement for structures within the clear zone of the road to have breakaway supports unless the sign is otherwise protected by guardrails (AASHTO 2017). The breakaway supports are weak by design as a driver safety measure to ensure a vehicle would break the sign support and safely pass beneath the sign without obstruction in the case of a collision. Given the usage of the same breakaway connections for the heavier electronic RICWS sign, the response of the sign structure to wind loading was reassessed in this study.

The main purpose of this work was to investigate the loading phenomena that may lead to premature failure of electronic RICWS signs. The investigation included both laboratory- and field-scale components. At the laboratory scale, a 1:18 geometric scale model of the RICWS sign structure was fabricated at St. Anthony Falls Laboratory (SAFL) to characterize the vortex shedding pattern and the drag and lift forces on the sign. At SAFL, the model RICWS drag properties were determined using a hydraulic channel facility as a towing tank, and the wake properties were measured in the wind tunnel facility. At the field scale, measurements of displacement and acceleration of the sign and the corresponding wind conditions were collected from an instrumented, full-size RICWS sign structure. The field data were used to characterize the natural and shedding frequencies of the system under various wind-loading conditions.

The integration of laboratory- and field-scale results allowed for (1) a thorough understanding of how unsteady wind loads affect the RICWS sign structure, and (2) a determination of the key design features leading to these effects. Based on the findings, adjustments to the design of the RICWS sign structure are proposed to help mitigate the effects of unsteady loads. The following section describes the experimental setup, including the field site, full-size and model-scale RICWS sign structures, and laboratory facilities. Results of the laboratory- and field-scale experiments follow with conclusions that generalize the results into a framework extending beyond the specific geometry of the RICWS sign.

Experimental Setup

RICWS Sign Structure, Field Conditions, and In Situ Measurements

The RICWS sign structure selected for the field campaign is shown in Figs. 1(a and b). The sign is located at the southwest corner of the intersection between Highway 7 and County Road 1 in McLeod, Minnesota (MnDOT 2015). The sign location was chosen due to the alignment of the sign with the prevalent wind direction and fairly undisturbed fetch along the same direction. The wind direction is reported relative to the face of the sign to account for the orientation (e.g., northerly winds corresponding to 0° were normal to the sign face). The mass of the main diamond-shaped electronic panel was approximately 35 kg. The total frontal area of the sign structure was 1.92 m², which included the diamond panel (1×1 m), rectangular plate (0.76×0.6 m), two light plates (each 0.46×0.46 m), and support posts (5 cm width). The sign was instrumented with two accelerometers attached to the back of the diamond face at a height of 3.6 m and two string potentiometers attached to the support posts from a separate post directly south of the sign at a height of 1.4 m. The accelerometers measured horizontal acceleration for the left and right side of the sign, and the potentiometers measured the position of the support posts relative to a fixed point 0.9 m in front of the sign structure. In addition, a cup and vane anemometer to measure wind speed and direction was situated west of the sign at a height of 2.5 m. The instrumentation is identified in Figs. 1(a and b).

Field data collection began in November 2017 and continued through August 2019. Acceleration and position data were collected continuously at a sampling frequency of 100 Hz, while wind speed and direction data were collected at a rate of 1 Hz. Under typical conditions, the only information saved from the raw data was average, maximum, and minimum measured values for each sensor in 5-min intervals. The 5-min data are referred to as *low frequency* (LF). When the wind speed at 2.5 m was above a specified threshold—above 7 ms⁻¹ for this study—the measurements were saved at the prescribed sampling frequency of 100 Hz (sign sensors) or 1 Hz (wind sensor). The purpose of the threshold for saving full-frequency data measurements was to reserve the limited data storage space for wind speed events more likely to cause large accelerations and displacements. The 7 ms⁻¹ threshold is approximately 1.5 times the average wind speed at 10 m in the region (Draxl et al. 2015), meaning it is an above-average wind speed with a high probability of occurring numerous times within the multi-year measurement campaign. The triggered, full-frequency events are referred to as the high-frequency (HF) data.

The position of the sign, as reported by the string potentiometers, did not always return to 0 when the sign was at rest. Over time, the resting position varied and slowly shifted to negative values, suggesting the sign was leaning increasingly toward the south

(from 4 mm in November 2017 to 12 mm in April 2018). Possible explanations for the shift include the effects of wind loading on the RICWS causing progressive displacements within the breakaway connection, or plowed snow and the frozen ground inducing seasonal variability and history effects. To account for the zero-displacement drift, a time-dependent resting position was used in place of a constant reference resting position. The estimated resting position was updated based on the measured sign position each time the wind speed was persistently close to zero. Displacements related to wind loading were then estimated as changes in the position from the most recent resting position.

Laboratory-Scale Model and Measurements

The laboratory-scale model RICWS sign structure, shown in Fig. 1(c), was fabricated using stainless steel components. The 1:18 scale with respect to the full-size sign was selected to allow the use of 6.4 mm (1/4-in.) rods as the model support posts. The model components, except for the two top light plates, were connected by welds. The light plates were attached with set screws which allowed them to be removed and reattached. The model was used in two types of laboratory experiments described below.

The SAFL main channel facility was used to investigate the drag and lift force characteristics of the RICWS sign structure. The channel was filled with quiescent water and used as a towing tank. The towing tank setup, designed by engineers at SAFL, is shown in Fig. 2(a). The RICWS model was mounted upside-down to a rod attached to five load cells which were calibrated prior to the experiment. Three cells measured force in the direction of the towing (F_x), and two cells measured in the transverse direction (F_y). The redundancy and positioning of the sensors were required to discriminate the forces from the moments. The load cell assembly was fixed to a motorized data acquisition carriage such that the RICWS model was only connected to the carriage through the load cells. The carriage was programmed to lower the mounted RICWS model into the water, tow the model through the channel at a prescribed velocity, and trigger acquisition of force measurements from the cells at 50 Hz during towing. Further details of the cart and instrumentation, including a diagram of the load cell assembly, are provided in the supplementary material of Musa et al. (2018). Given the immersed sign moving through the quiescent water at constant velocity, this experiment featured spatially uniform and laminar incoming flow conditions.
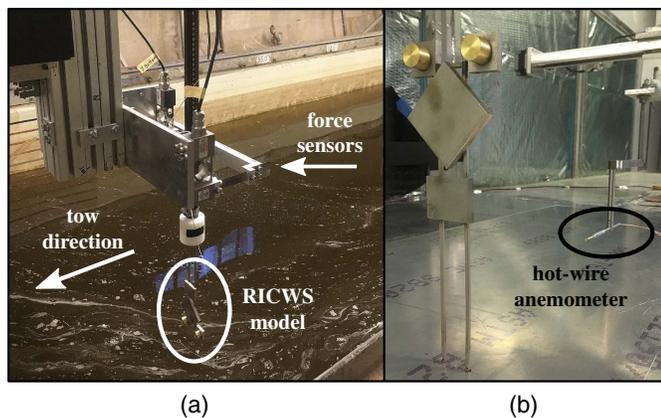
The SAFL atmospheric wind tunnel was used to investigate the behavior of the RICWS sign structure under turbulent boundary layer inflow conditions that are more representative of the field site as compared to the uniform inflow of the towing tank facility. In this experiment, the model RICWS sign structure was mounted on the floor of the wind tunnel. The wind tunnel test section has a cross section of 1.7×1.7 m and 16 m of fetch downwind of the inlet. The tunnel fetch allows for fully-developed, zero-pressure-gradient, turbulent boundary layer flow conditions within the test section. An 8-cm picket fence was used at the inlet to increase the boundary layer thickness such that the boundary layer exceeded the RICWS model height and the entire model was exposed to the mean shear of the turbulent inflow, consistent with field conditions. Flow velocities were measured using hot-wire anemometry at a frequency of 10 kHz. A traverse system was used to position the hot-wire sensor at specific points in the wake of the RICWS model along the vertical direction and aligned with the horizontal center of the sign (i.e., $y = 0$). The hot-wire anemometer and traverse system are shown downstream of the RICWS model in Fig. 2(b). See Chamorro and Porté-Agel (2009) and Howard et al. (2015) for more details on the SAFL wind tunnel facility and measuring system.

Laboratory-Scale Results

Drag and Lift Coefficients

Towing tank force measurements were acquired for a range of towing velocities from $U = 0.3$ to 1.0 ms^{-1} and various orientations of the sign with respect to the towing direction. The orientations resulted in effective flow directions θ varying from 0° to 180°. Consistent with the field measurements, $\theta = 0°$ corresponds to a flow direction normal to the sign face. Selected experiments were also conducted with the two light plates removed from the model.

The force that a fluid imparts on an immersed solid area is defined by the relationship $F_x = (1/2)C_x \rho A U^2$. The relationship can be rearranged to determine the force coefficients of the model RICWS sign structure:
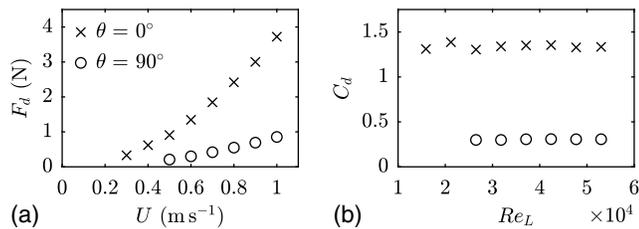
$$C_x = \frac{2F_x}{\rho A U^2} \tag{1}$$

where C_x = coefficient for drag C_d or lift C_L; F_x = corresponding measured drag or lift force; ρ = fluid density; A = total frontal area of the sign; and U = inflow (towing) velocity. Contributions to the area A include the diamond face, rectangular plate, and two light plates shown in Fig. 1(c). The support posts were assumed to have a negligible effect on the area.

The force coefficient C_x is expected to depend on the sign geometry and the Reynolds number (Munson et al. 2012). The Reynolds number is defined using a characteristic velocity and length, and in this case is

$$Re_L = \frac{UL}{\nu} \tag{2}$$

where L = length of the diamond face as shown in Fig. 1(c); and ν = kinematic viscosity of the fluid. For general bluff bodies immersed in a uniform flow, when the Reynolds number is sufficiently high, C_x becomes independent of Re_L and is only a function of the geometry in relation to the flow direction (Munson et al. 2012). Fig. 3 shows the measured drag force F_d and calculated drag coefficient C_d for the cases when the flow was perpendicular ($\theta = 0°$) and parallel ($\theta = 90°$) to the sign face. The average drag coefficient values

Fig. 2. Laboratory experiments using the model RICWS sign structure: (a) towing tank experiment to measure drag and lift forces; and (b) wind tunnel experiment to measure wake characteristics.

Fig. 3. Drag force parameters of the model RICWS sign structure for flow direction $\theta = 0°$ (perpendicular to the sign face) and 90° (parallel): (a) drag force F_d; and (b) drag coefficient C_d.

were $C_d = 1.34 \pm 0.07$ for $\theta = 0°$ and $C_d = 0.30 \pm 0.05$ for $\theta = 90°$. The uncertainty ranges are the result of 2% uncertainty in the calibration of the force sensors and of the difference in C_d values between the tested U cases. As seen by the constant values in Fig. 3(b), the drag coefficient was independent of the Reynolds number for the range of Re_L investigated.

Fig. 4 shows the drag and lift parameters of the model RICWS sign for a range of flow directions. The greatest drag force occurred for $\theta = 0°$ and 180° when the flow was perpendicular to the sign face, which was expected due to the largest projected sign area normal to the flow. The drag coefficient is maximum for the same flow directions due to the largest pressure difference between the front and back of the sign resulting in the strongest form drag contribution. The lift coefficient, corresponding to the force perpendicular to the flow direction, is negligible at $\theta = 0°$, 90°, and 180° and largest in the ranges $\theta = 45°–60°$ and $\theta = 120°–135°$. The drag and lift relationships in Fig. 4 are consistent with previous studies of forces on flat plates (Ortiz et al. 2015).

The effect of the two square light plates on the RICWS drag response was tested by comparing forces with and without the plates removed. Removing the light plates decreased the drag force by an amount comparable to the area removed from the structure. The small increase in the drag coefficient to $C_d = 1.40 \pm 0.07$ was within the experimental uncertainty of the estimates. Efforts to reduce the sign area such as by removing the lights can be expected to lead to a proportional decrease in the drag force and to lessen the dynamic response of the sign.

Frequency Response

In general, the oscillatory behavior of the RICWS sign structure was expected to reveal two primary frequency components associated with the elastic characteristics of the structure, i.e., the natural frequency and an aerodynamic forcing mechanism such as vortex shedding. The natural frequency is a function of the structural stiffness and mass and is independent of the external forcing. As described in the introduction, the vortex shedding frequency is governed by the Strouhal number

$$St = \frac{f_v L}{U} \qquad (3)$$

where f_v = vortex shedding frequency; L = length of the diamond face of the sign; and U = incoming flow velocity. The selection of the diamond side length L as the key characteristic length scale in the Strouhal and Reynolds numbers was a posteriori in order to match later results to the vortex shedding frequency $St = 0.2–0.3$ observed for a wide range of geometries and applications (Lienhard 1966; Lam and Wei 2010; Heisel et al. 2018). The length scale can be determined a priori for simple geometries, e.g., the diameter is the relevant length for a cylinder. For more complex cases with multiple individual geometries such as the RICWS sign structure, the vortex shedding length scale likely corresponds to the largest blockage element and can be confirmed experimentally. Similar to the drag coefficient, the Strouhal number is typically independent of the Reynolds number (Berger and Wille 1972; Heisel et al. 2018). It was therefore expected that the shedding frequency identified at the laboratory scale would be representative of the field site with the Strouhal scaling applied. Note that using the vertical extent of the diamond plate for L instead of the side length would increase the observed Strouhal value but would not affect the estimated field-scale shedding frequency f_v due to the geometric consistency of the model, i.e., St/L would be the same.

Oscillations of the sign structure resulting from the natural and vortex shedding frequencies can be detected in the temporal signal of the forces. The energy spectral density Φ, also known as the power spectrum, was used to investigate the frequency response of the force measurements. The power spectrum Φ represents the energy of fluctuations as a function of the frequency, where the fluctuations are deviations from the mean value. Frequencies representing the primary oscillations of the structure appear as peaks in the spectrum. The peaks may correspond to either the natural frequency f_o or the shedding frequency f_v. The fast Fourier transform was used to estimate the power spectrum of the force fluctuations Φ_F, where the power spectrum is the square of the transform. Welch's method was used to reduce noise in the estimated spectrum; separate spectra were calculated on segments of the data series, and the spectra were averaged to produce the final estimate (Welch 1967). The integral of the spectrum is equal to the variance of the signal such that normalizing by the variance yields a spectrum with an integral of unity.

Fig. 5(a) shows a sample normalized drag force spectrum Φ_F. To determine whether the energy peaks near $f = 4$ and 10 Hz were the natural or shedding frequencies, Φ_F must be estimated for a range of velocities as shown in Fig. 5(b). The plot in Fig. 5(c) depicts Φ_F as a function of both frequency and velocity, with the tone (or shade) corresponding to the Φ_F value. The smaller peak near $f = 10$ Hz is independent of the flow velocity U, indicating it is the natural frequency of the model RICWS sign structure. Note that the natural frequency of the model is not expected to be equal to that of the full-size RICWS sign structure.
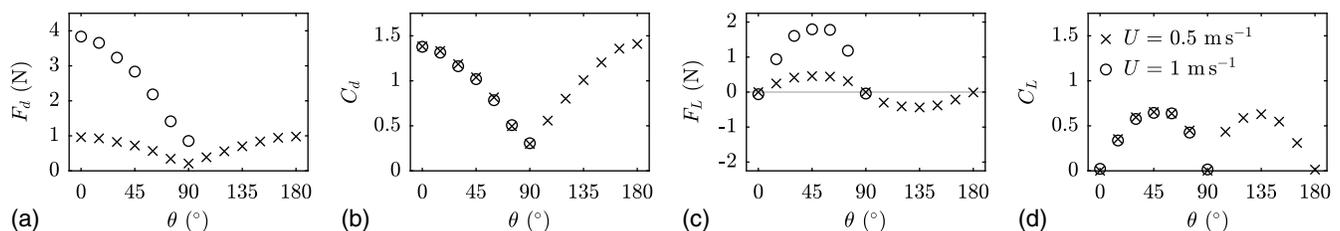

Fig. 4. Drag and lift parameters of the model RICWS sign as a function of flow direction θ for two inflow speeds: (a) drag force F_d; (b) drag coefficient C_d; (c) lift force F_L; and (d) lift coefficient C_L.
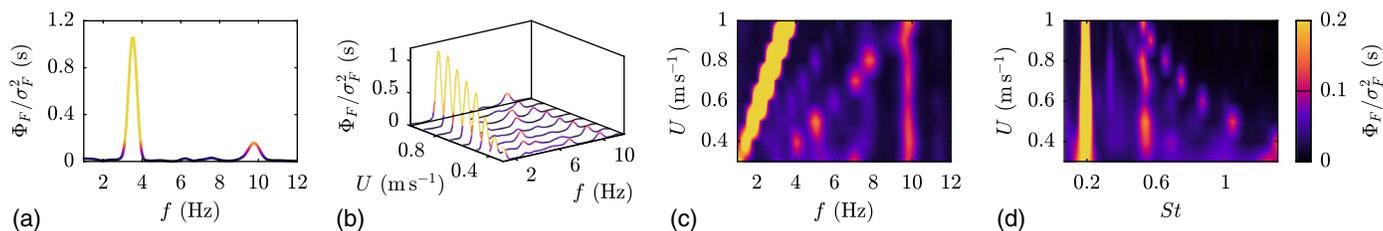
Fig. 5. Estimated power spectrum of the drag force fluctuations Φ_F on the model RICWS sign structure: (a) power spectrum for $U = 1$ ms^{-1}; (b) spectra for each measured velocity; (c) planar view of b, where values between the measured U are interpolated; and (d) same as c, except frequency is normalized as the Strouhal number $St = fL/U$.

The stronger peak in the range $f = 2$–4 Hz in Fig. 5(c) changes with velocity. When the frequency is normalized as the Strouhal number as in Fig. 5(d), the stronger peak becomes invariant at a value centered at $St = 0.19$. The spectral signature near $St = 0.2$ confirms the presence of vortex shedding governed by the Strouhal number and validates the choice of L. The weaker shedding signatures at $St = 0.33$ and 0.55 correspond to the rectangular plate and the two light plate geometries, respectively. This is confirmed by achieving $St = 0.2$ for each peak when redefining St using the heights of the rectangular and light plates as the characteristic lengths in Eq. (3).

The effect of the flow direction on the resulting force oscillations is demonstrated in Fig. 6. The primary vortex shedding at $St = 0.19$ induces forces in the flow direction as seen in Fig 6(b), but based on the lack of a spectral signature in Fig. 6(c) the shedding does not result in transverse force oscillations. Rather, the transverse force spectrum indicates excitation at the natural frequency around $f = 9$ Hz. The small differences in natural frequency between Figs. 5 and 6 (and in the later wind tunnel testing) may be due to minor changes in the height of the support posts when the posts were secured for the various experimental runs. To assess forces in the same reference frame as the field measurements, a rotation matrix was used to calculate the forces perpendicular to the RICWS sign structure face as shown in Fig. 6(d). Vortex shedding was responsible for the force fluctuations when the flow was perpendicular to the structure (i.e., $\theta \cong 0°$ or $180°$), but a separate mechanism which excites the natural frequency is more relevant for parallel flow conditions ($\theta \cong 90°$ or $270°$). These direction trends are further discussed in the section on field-scale results.

According to aerodynamic theory, vortex shedding should induce force oscillations with frequency f_v in the transverse y direction and frequency $2f_v$ along the flow direction x. These frequencies were first observed experimentally for simple geometries such as a cylinder (McGregor 1957; Surry 1972), and they result from vortex pairs alternately detaching from opposite sides of the geometry. In the case of the more complex RICWS geometry, the flow was expected to accelerate between the two square light plates at the top of the structure such that the primary vortex likely formed at the top point of the diamond face [see, e.g., Zhu et al. (2020)]. The rectangular plate below the diamond prevented a corresponding vortex on the opposite (bottom) point of the diamond. The lack of a vortex pair led to drag force oscillations along the x-direction at frequency f_v, as seen in Fig. 5, rather than $2f_v$. The orientation of the vortex in the streamwise-vertical $x − z$ plane explains the lack of a vortex shedding signature in the spanwise force F_y in Fig. 6(c). The following wind tunnel analysis was used to confirm the shedding frequency f_v.

Power spectra were estimated for the wind tunnel experiment with turbulent inflow conditions using the streamwise velocity signal in the wake of the model RICWS sign structure. The vortices shed by the structure result in the same spectral signature in the wake velocity as in the drag forces. The wake velocity was measured for three cases: a high velocity of the free-stream region above the boundary layer U_∞, a lower free-stream velocity U_∞, and a low sign height (at the higher U_∞). The free-stream velocity was controlled by the fan speed of the wind tunnel. The height of the model support posts scaled with the full-size RICWS sign structure in the first two wake cases and the towing tank test, and the third wake case assessed the effect of shorter support posts. Figs. 7(a and b) show the inflow and wake velocity profiles, with the sign height included for reference. From the profiles, the velocity deficit in the RICWS sign structure wake is evident, as is the boundary layer inflow condition.

Power spectra of the velocity fluctuations Φ_u for the wake cases and inflow are shown in Fig. 7(c). The wake spectra are based on measurements at a single point $2L$ downstream from the center of the diamond-shaped panel. The inflow spectra are from measurements at the same height. Compared to the laminar inflow conditions for the towing tank test, the turbulent boundary layer inflow
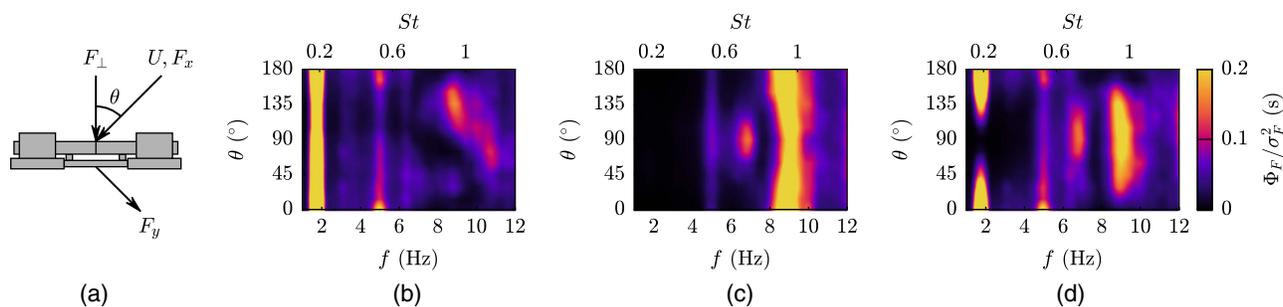

Fig. 6. Force power spectrum Φ_F as a function of flow direction θ for $U = 0.5$ ms^{-1}: (a) top view of the model structure showing the force notation; and spectra for forces (b) in the flow direction F_x; (c) transverse to the flow F_y; and (d) perpendicular to the structure face $F_\perp$.
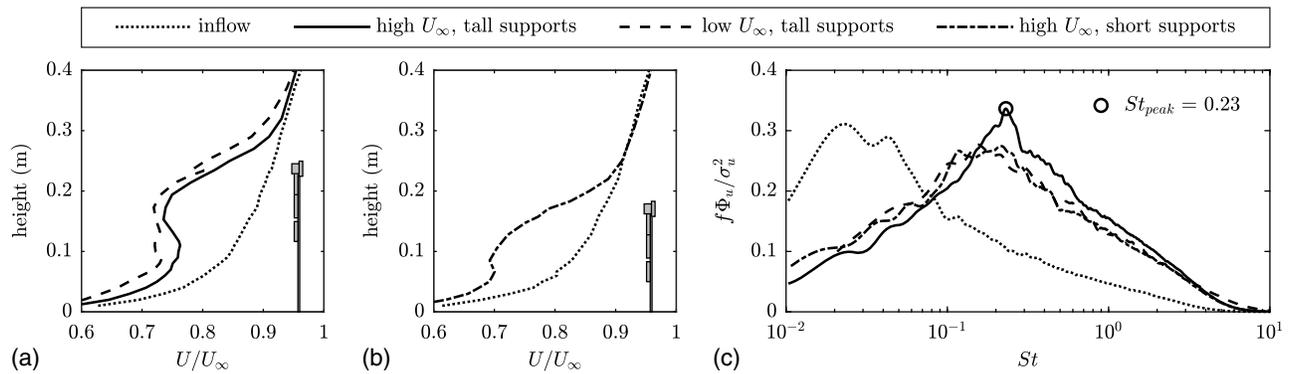
Fig. 7. Wake properties of the model RICWS sign structure: (a, b) mean wake velocity profiles U for the three experimental cases; and (c) premultiplied power spectrum of the velocity fluctuations Φ_u for the three cases.

already had significant (kinetic) energy in the velocity fluctuations. Turbulent fluctuations across a wide range of scales in the inflow conditions lead to more complex fluid-structure and wake interactions and a broader spectral peak centered at $St = 0.23$. A small increase in the Strouhal number is expected when the inflow conditions change from nonturbulent to turbulent (Knisely 1990; Sun et al. 2014). The Strouhal number of the full-size RICWS sign structure was therefore expected to be closer to the value observed in the wind tunnel than in the towing tank. Note that the spectral peak identified for the wake velocity is a direct estimate of the vortex shedding frequency f_v, thus supporting the assumptions regarding both the choice of L and the frequency of the unsteady drag force component F_x induced by vortex shedding.

To analyze the vibrations of the model RICWS sign structure in the wind tunnel, 120 Hz video was captured of the side of the model. By detecting the position of sign features in each video frame, a time signal of the sign displacement Δx was constructed as shown in Figs. 8(a and b). Power spectra of the displacement Φ_x for the three wind tunnel cases are shown in Fig. 8(c). The detected spectral peak in each case corresponded to the natural frequency of the sign. The peak for the higher sign height above $f = 8$ Hz was close to the natural frequency detected from the towing tank test. As expected, higher wind velocity leads to larger displacements. Reducing the sign height increased the stiffness, which led to a likewise increase in the natural frequency.

Field-Scale Results

Because the drag coefficient and Strouhal number were observed to be invariant of the Reynolds number, the values determined through laboratory-scale testing were directly applied in the analysis of the full-size RICWS sign structure. The drag coefficient was used to approximate the average wind load under different measured wind velocities. The unsteadiness of the wind load resulting from the vortex shedding frequency was estimated from the Strouhal relationship. The natural frequency f_o of the model-scale RICWS sign structure could not be used to predict the field-scale value. The natural frequency depends on the sign materials, mechanical properties of the structural supports and joints, mass distribution, and soil conditions. These properties were not all consistent between the model-scale and full-size RICWS sign structure. The natural frequency was instead estimated using the HF field measurements as described later in this section.

The average sign response was determined for a range of wind conditions measured by the cup and vane anemometer. Fig. 9(a) shows the average horizontal displacement Δx as a function of the relative wind direction θ for both the 5-min averaged LF data and the triggered HF wind event data. The largest magnitude displacements corresponded to flow perpendicular to the sign face, i.e., $\theta \cong 0°$ and 180°. This was expected due to the drag force being largest in these directions (Fig. 4) and the assumed relationship between the drag force and displacement. Figs. 9(b and c) show wind roses of the wind events responsible for the largest class of negative and positive displacements, respectively. The wind roses represent the distribution of wind speed and direction associated with the high-displacement events. Consistent with Fig. 9(a), the positive displacement events are due to winds primarily from the south of the sign ($\theta \approx 150°$), and northerly winds ($\theta \approx 20°$) are responsible for the negative displacement events. Higher wind speeds occurred for winds from the north, which explains the larger average
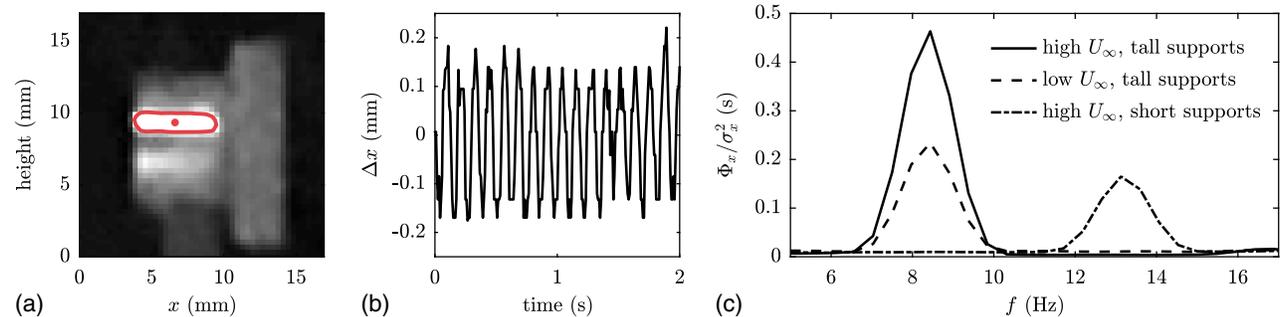

Fig. 8. Vibration analysis of the model sign structure in the wind tunnel: (a) example video frame indicating the detected reflection centroid; (b) example time series of centroid displacement Δx; and (c) power spectra of the displacement fluctuations Φ_x.
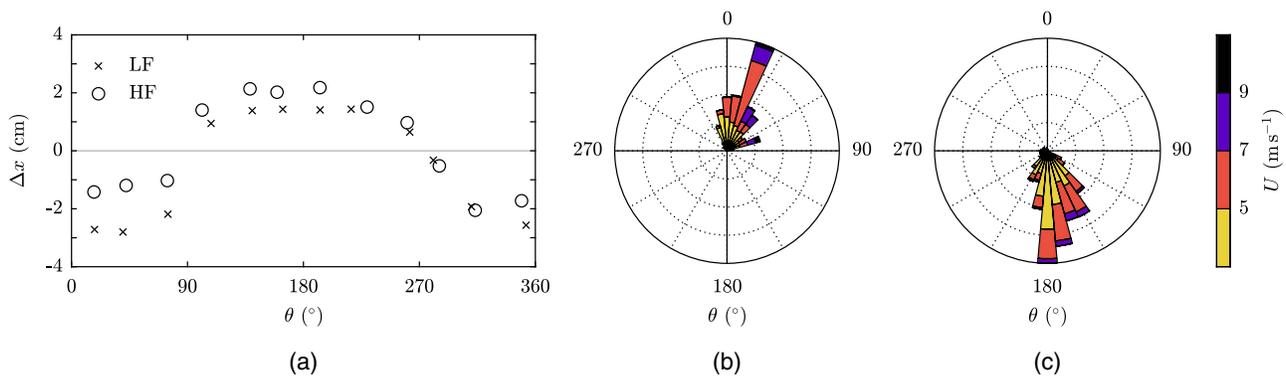
Fig. 9. Relationship between wind direction θ and horizontal displacement Δx of the field-scale RICWS sign structure: (a) average displacement for the LF and HF data; and wind roses for wind events corresponding to (b) $\Delta x < -3$ cm and (c) $\Delta x > 1.5$ cm.

displacement for northerly winds in Fig. 9(a). Based on the wind rose distributions, analysis of the field data focused on the northerly and southerly wind events responsible for the largest horizontal displacements.

Stiffness Determination

The simplest physical model to predict the natural frequency requires the structural stiffness, which can be estimated in the field assuming a linear elastic force-displacement constitutive equation. The main assumption is static equilibrium between the drag force and the elastic response of the sign structure. The force and stiffness k are then related as

$$F_d = \frac{1}{2} C_d \rho A U^2 = k \Delta x \tag{4}$$

where C_d = drag coefficient estimated in the laboratory experiment and shown to be independent of Reynolds number (Fig. 3); ρ = density of air; A = total frontal area of the RICWS sign structure; U = measured wind speed; and Δx = horizontal displacement at the centroid of the diamond plate. The centroid of the diamond plate was chosen as the representative location at which the wind drag force would be applied, because it corresponded to the region of maximum velocity deficit from the wind tunnel experiment and was the blockage element responsible for the largest vortex shedding response in the towing tank test. The displacement at the centroid of the diamond plate was extrapolated linearly from the displacement measured at the height of the string potentiometers. To estimate k from the LF displacement data, only events with wind speeds greater than 6 ms^{-1} and northerly ($-40° < \theta < 40°$) or southerly ($140° < \theta < 220°$) direction were

considered. Fig. 10 shows the relationship between the measured (squared) wind velocity U^2 and displacement Δx for the wind events meeting these criteria. The slope of the relationship in Fig. 10 can be expressed as $(1/2) C_d \rho A / k$ from Eq. (4), with k being the only unknown in the slope expression; the stiffness was determined from linear fit of the points in Fig. 10.

The displacement data of Potentiometer Sensor 2 appeared to estimate a slightly smaller stiffness as compared to Sensor 1, which might be due to slightly different string mounting on the two posts. Also, relatively short-term variations in the zero-displacement position of the potentiometer sensors may have occurred due to changes in the temperature and water/ice content of the soil and possible backlash or slop at the base of the breakaway connection. Due to uncertainty in the resting position under the varying conditions, the linear fit of the data did not impose the intercept to be at the origin. The difference in reference displacement is evident in Figs. 10(b and d) with the vertically offset linear trends in the clusters of displacement data from southerly winds. The two clusters were analyzed separately, resulting in two southerly and one northerly datasets. For each of the three datasets, an individual linear fit was determined for the two sensors using both the scattered data and binned averaging, leading to 12 estimated values of the stiffness. The mean stiffness resulting from the fits was $k = 3,300$ N · m^{-1} and the standard deviation was $\sigma_k = 370$ N · m^{-1} (excluding one outlier at 8,300 N · m^{-1}). The mean and standard deviation of the stiffness were used in the following section to estimate a range of expected natural frequencies.

Frequency Response

Spectral analysis of the HF (100 Hz) displacements and accelerations measured during triggered wind events was used to determine
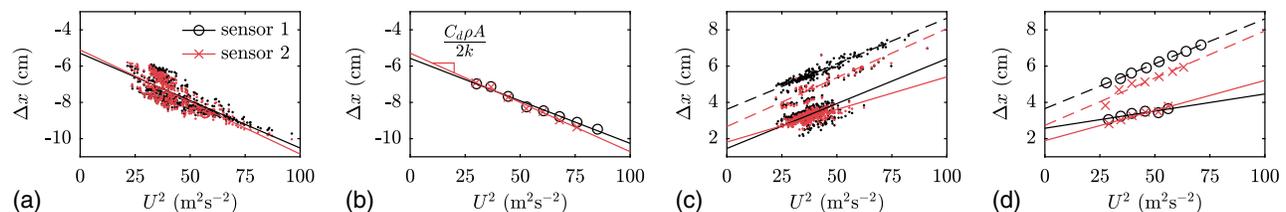

Fig. 10. Horizontal displacement Δx of the field-scale RICWS sign structure used to estimate the stiffness k: linear fits to northerly wind events using (a) scattered data and (b) binned averages; and (c, d) same as a and b, but for southerly wind events. Displacement Δx was estimated using the LF data of two string potentiometers (i.e., Sensors 1 and 2). Southerly wind events in c were separated into two data clusters characterized by different residual displacements and each cluster was individually fitted (i.e., dashed and solid line).
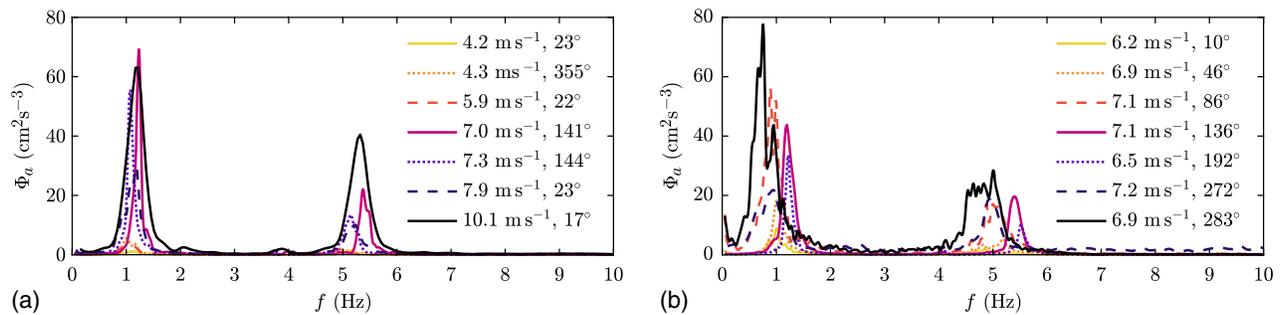
Fig. 11. Estimated power spectra of acceleration Φ_a for the field-scale RICWS sign structure: (a) for varying wind speed and northerly wind direction; and (b) for varying wind direction and similar wind speed.

the natural frequency of the full-size RICWS sign structure and understand the role of vortex shedding. The effects of wind speed and direction were investigated by comparing spectra for a combination of wind events with varying wind speed and direction. The spectra were estimated using Welch's method in the same manner as the laboratory case. Fig. 11(a) shows the power spectrum of acceleration fluctuations Φ_a for seven wind events with varying wind speed ($U = 4.1$–10 ms^{-1}) and direction within $40°$ of normal to the sign face (i.e., $\theta = 0° \pm 40°$ or $\theta = 180° \pm 40°$). Conversely, Fig. 11(b) shows Φ_a for seven wind events with varying wind direction ($\theta = 10°$–$283°$) and similar speeds ($U = 6.1$–7.2 ms^{-1}). Both plots reveal a primary spectral peak near $f = 1$ Hz and a secondary peak around $f = 5$ Hz regardless of the wind conditions. The invariance of the peaks with respect to wind speed and direction supports the interpretation of the peaks as natural vibrational modes of the sign.

The primary peak can be compared to the anticipated natural frequency by considering the system as a mass m attached to a spring with stiffness k. The natural frequency of this simplified system is

$$f_o = \frac{1}{2\pi} \sqrt{\frac{k}{m}} \tag{5}$$

Using the average stiffness determined from the LF displacement data and the total mass of the sign $m = 40$ kg, the expected natural frequency was $f_o = 1.4 \pm 0.13$ Hz, which corresponded closely with the primary peaks in Fig. 11. Note that the simplified model of Eq. (5) assumes that the force and the mass have the same centroid through which the single degree of freedom is defined, implying that the displacement location used to estimate the stiffness is not arbitrary. The drag force is inferred to apply where the pressure difference between the two sides of the sign is highest. This is located at the center of the diamond panel based on the observed maximum velocity deficit in the wake of the diamond panel seen in Figs. 7(a and b). In the specific case of the RICWS geometry, the drag contribution of the lower panel was likely balanced by the higher wind velocity on the diamond and light panels.

The second peak at $f = 5$ Hz corresponded to the dominant torsional mode. The accelerometers were out of phase at this frequency, which indicated twist of the electronic sign panel. Based on a finite element model of the system (Zhu et al. 2020), this mode likely also included lateral deformations.

The frequencies of the most prominent spectral peaks are represented in Fig. 12 for both the acceleration spectra from Fig. 11 and the horizontal displacement spectra (not shown) based on the same wind events. Fig. 12 shows the frequency peaks for each wind event as a function of the average wind speed U and the average wind direction θ. Based on the frequency peak in the wake

experiment results (e.g., Fig. 7), the vortex shedding frequency f_v at the field scale was estimated using $St = 0.23$ and Eq. (3). Fig. 12(a) includes f_v estimates based on the diamond plate size L and the recorded wind speed for each event. The plot reveals significant overlap between the vortex shedding frequency and the apparent natural frequency. From a structural perspective, the alignment of the frequencies allows the forcing frequency from the unsteady wind loads to excite the natural frequency of the structure, leading to resonance, fatigue, and potential failure.

The overlap of frequencies occurs for high wind speeds ($U = 6$–8 ms^{-1}) which corresponds to larger unsteady wind loads ($F \sim U^2$) and more energy in the frequency response. In Fig. 11(a), the spectral peak increased from $\Phi_{peak} = 2$ cm^2 s^{-3} for $U = 4$ ms^{-1} to $\Phi_{peak} = 80$ cm^2 s^{-3} for $U = 7$ ms^{-1}. Along with the overall acceleration variance, the peak frequency response increased considerably with wind speed due to the increased drag force and the alignment of the vortex shedding frequency.

In addition to the wind speed, the energy in the frequency response was also dependent on the wind direction. Fig. 13 shows the standard deviation of the horizontal displacement σ_x and the peak amplitude of the acceleration spectra Φ_{peak} as functions of the wind direction. While the largest average displacements occurred with winds perpendicular to the sign face (Fig. 9), the trends in Fig. 13 suggest that oscillations at the natural frequency increased when the wind was close to parallel to the sign face (i.e., $\theta \cong 90°$ or $270°$). This effect is consistent with the laboratory-scale direction trends in Fig. 6, in which the natural frequency response was particularly relevant under parallel flow conditions. The increased displacement oscillations for parallel wind events may be due to backlash in the structural support bases, which was observed during visits to the instrumented sign; the supports provided limited resistance to displacement when the RICWS sign structure was nearly vertical, which was more likely to occur for parallel wind events.
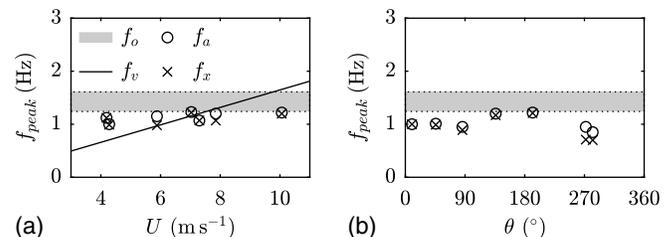

Fig. 12. Observed peak energetic frequencies for acceleration f_a and displacement f_x of the field-scale structure compared with the uncertainty range of the natural frequency f_o and the estimated vortex shedding frequency f_v.
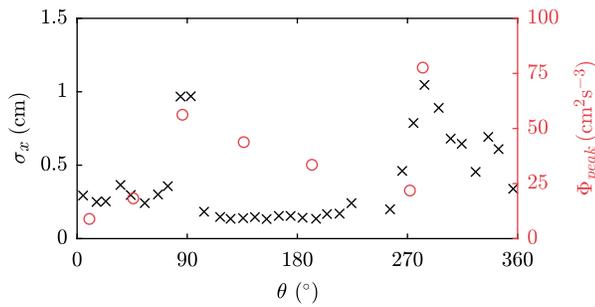
Fig. 13. Standard deviation of the oscillating displacement σ_x and acceleration spectrum peak Φ_{peak} for the field-scale RICWS sign structure as a function of the wind direction θ.

Under perpendicular flow conditions, the mean drag force displaces the structure until the support bases provide greater resistance to further displacements. In addition to the backlash, a forcing mechanism is required to induce the observed displacements. The towing tank results suggested that the forcing mechanism must act transverse to the flow direction, indicating a possible relationship to the lift force. These characteristics—lift force oscillations self-excited at the natural frequency—are consistent with an aeroelastic instability such as flutter (Simiu and Yeo 2019), but there is insufficient evidence here to conclusively confirm the nature of the mechanism. The displacements during parallel wind events may also have been induced by atmospheric turbulence, which has energetic velocity fluctuations in all directions (Raupach et al. 1991). Turbulent velocity fluctuations transverse to the flow and short-term variability in the wind direction can both produce lift force (F_y) oscillations, leading to periodic displacement of the structure, which may be amplified if they are close to the natural frequency.

Discussion and Conclusion

Laboratory experiments and field monitoring were used to study the mechanical behavior of the RICWS sign structure exposed to a representative range of wind conditions observed during a full year of measurements. The field observations included measurements of strain, acceleration, and wind speed. The laboratory experiments comprised wind tunnel testing for the sign model wake unsteadiness and towing tank testing for the estimates of the drag coefficient and the oscillations of the drag and lift forces.

By comparing the unsteady drag forces on the sign with the measured peak of the wake velocity spectrum, we confirmed statistically that vortices shed into the wake of the sign are responsible for the primary unsteady forces on the structure. The frequency of this vortex shedding is governed by the flow velocity and the sign geometry, which together are described by the dimensionless Strouhal number. The Strouhal number for the RICWS sign structure, based on the size of the largest sign panel, is $St = 0.23$. This value is consistent with simpler geometries such as a cylinder, suggesting that the shedding frequency for complex-shaped structures such as roadside signs can be predicted based on the geometry of the largest blockage element and the incoming wind speed.

The invariance of the Strouhal number with respect to the Reynolds number, for the laboratory conditions tested, allowed extending the predicted vortex shedding frequency to the full-size RICWS structure. At the field scale, for high wind speeds (i.e., $U = 6$–8 ms^{-1} at 2 m above the ground, compared to the average wind speed $U = 2$ ms^{-1}), the vortex shedding frequency matched the natural frequency of the sign identified based on the primary

energetic peak in the acceleration spectra. The matching frequencies suggest resonance conditions and potential structural failure. Vortex shedding is not typically addressed in the standard design of roadside sign supports. Our findings demonstrate the need for these standards to consider vortex shedding, particularly as the inclusion of electronic signage makes the structures heavier and more expensive.

While most of our measurements were focused on the sign structure configuration perpendicular to the wind, our field observations on wind directionality suggest that the vibrational behavior of the sign changes drastically when the wind is almost parallel to the planar structure. We confirmed the directional change in behavior in the towing tank testing. In such a specific case, the out-of-plane lift force oscillations and associated displacements may be predominantly governed by the spanwise variability of the turbulence flow, rather than by vortex shedding, thus making resonance prediction more uncertain. It is therefore necessary to test the vibrational response across a range of directions in experiments or simulations to fully characterize the unsteady forces on such structures.

By approximating the structure as a single degree of freedom system, and by equating the vortex shedding and natural frequency expressions, the following estimate is reached for the wind speed corresponding to resonant conditions: $U_{res} \approx L\sqrt{k/m}/(2\pi St)$. Several design constraints of the RICWS sign structure cause the resonant wind speed U_{res} to overlap with frequently occurring, above-average wind conditions. Visibility requirements include the two flashing lights and the sign height. The two flashing lights increase the total frontal area, total mass, and height of the center of mass of the sign. The electronic signage of the diamond plate also increases the sign mass. The sign face must be more than 2.5 m above the road level for visibility purposes, which decreases the stiffness compared to shorter signs. The stiffness is also constrained by the breakaway supports required for driver safety during a collision.

Despite the aforementioned restrictions, design options exist to mitigate the overlap of the vortex shedding and natural frequencies within the operating wind speed range. Affordable retrofitting options, which are applicable to any roadside sign design, include: (1) reducing the blockage area without compromising the visibility (e.g., reduce area of flashing lights and material surrounding the lights); (2) including vibration dampers common to larger structures (Christenson and Hoque 2011; Giaralis and Petrini 2017); (3) reducing backlash in the base supports; and (4) implementing aerodynamic modifications to mitigate vortex shedding or dilute the range of the excited frequencies (Zhu et al. 2020).

Regardless of the engineering solution, there is a need for vortex shedding and similar unsteady aerodynamics to be addressed in the standard guidelines for increasingly complex roadside structures. Using the RICWS sign structure as an example, we outlined here several experimental procedures to help better understand these unsteady aerodynamics for other roadside signs or complex geometries.

Data Availability Statement

Data and code generated or used during the study are available from the corresponding author by request.

References

AASHTO. 2017. *LRFD specifications for structural supports for highway signs, luminaries, and traffic signals*. Washington, DC: AASHTO.

Amy, R. A., G. S. Aglietti, and G. Richardson. 2009. "Reliability analysis of electronic equipment subjected to shock and vibration—A review." *Shock Vib.* 16 (1): 45–59. https://doi.org/10.1155/2009/546053.

Berger, E., and R. Wille. 1972. "Periodic flow phenomena." *Annu. Rev. Fluid Mech.* 4 (1): 313–340. https://doi.org/10.1146/annurev.fl.04.010172.001525.

Bokaian, A., and F. Geoola. 1984. "Vortex shedding from two interfering circular cylinders." *J. Eng. Mech.* 110 (4): 623–628. https://doi.org/10.1061/(ASCE)0733-9399(1984)110:4(623).

Chamorro, L. P., and F. Porté Agel. 2009. "A wind-tunnel investigation of wind-turbine wakes: Boundary-layer turbulence effects." *Boundary Layer Meteorol.* 132 (1): 129–149. https://doi.org/10.1007/s10546-009-9380-8.

Chang, B., B. M. Phares, P. P. Sarkar, and T. J. Wipf. 2009. "Development of a procedure for fatigue design of slender support structures subjected to wind-induced vibration." *Transp. Res. Rec.* 2131 (1): 23–33. https://doi.org/10.3141/2131-03.

Chen, Z. Q., X. D. Yu, G. Yang, and B. F. Spencer. 2005. "Wind-induced self-excited loads on bridges." *J. Struct. Eng.* 131 (12): 1783–1793. https://doi.org/10.1061/(ASCE)0733-9445(2005)131:12(1783).

Christenson, R. E., and S. Hoque. 2011. "Reducing fatigue in wind-excited support structures of traffic signals with innovative vibration absorber." *Transp. Res. Rec.* 2251 (1): 16–23. https://doi.org/10.3141/2251-02.

Connor, R. J., S. H. Collicott, A. M. DeSchepper, R. J. Sherman, and J. A. Ocampo. 2012. *Fatigue loading and design methodology for high-mast lighting towers*. NCHRP Rep. No. 718. Washington, DC: Transportation Research Board.

Draxl, C., A. Clifton, B. M. Hodge, and J. McCaa. 2015. "The wind integration national dataset (WIND) toolkit." *Appl. Energy* 151 (Aug): 355–366. https://doi.org/10.1016/j.apenergy.2015.03.121.

Garlich, M. J., and E. T. Thorkildsen. 2005. *Guidelines for the installation, inspection, maintenance and repair of structural supports for highway signs, luminaries, and traffic signals* Rep. No. FHWA NHI 05-036. Washington, DC: Federal Highway Administration.

Giaralis, A., and F. Petrini. 2017. "Wind-induced vibration mitigation in tall buildings using the tuned mass-damper-inerter." *J. Struct. Eng.* 143 (9): 04017127. https://doi.org/10.1061/(ASCE)ST.1943-541X.0001863.

Heisel, M., J. Hong, and M. Guala. 2018. "The spectral signature of wind turbine wake meandering: A wind tunnel and field-scale study." *Wind Energy* 21 (9): 715–731. https://doi.org/10.1002/we.2189.

Hong, H. P., G. G. Zu, and J. P. C. King. 2014. "Reliability consideration for fatigue design of sign, luminaries, and traffic signal support structures under wind load." *J. Wind Eng. Ind. Aerodyn.* 126 (Mar): 60–74. https://doi.org/10.1016/j.jweia.2013.12.012.

Hosch, I. E., and F. H. Fouad. 2009. "Fatigue design of sign support structures for loading caused by natural wind loads." *Transp. Res. Rec.* 2131 (1): 15–22. https://doi.org/10.3141/2131-02.

Howard, K. B., J. S. Hu, L. P. Chamorro, and M. Guala. 2015. "Characterizing the response of a wind turbine model under complex inflow conditions." *Wind Energy* 18 (4): 729–743. https://doi.org/10.1002/we.1724.

Kareem, A., L. Hu, Y. Guo, and D. K. Kwon. 2019. "Generalized wind loading chain: Time-frequency modeling framework for nonstationary wind effects on structures." *J. Struct. Eng.* 145 (10): 04019092. https://doi.org/10.1061/(ASCE)ST.1943-541X.0002376.

Kareem, A., and T. Wu. 2013. "Wind-induced effects on bluff bodies in turbulent flows: Nonstationary, non-Gaussian and nonlinear features." *J. Wind Eng. Ind. Aerodyn.* 122 (Nov): 21–37. https://doi.org/10.1016/j.jweia.2013.06.002.

Knisely, C. W. 1990. "Strouhal numbers of rectangular cylinders at incidence: A review and new data." *J. Fluids Struct.* 4 (4): 371–393. https://doi.org/10.1016/0889-9746(90)90137-T.

Lam, K. M., and C. T. Wei. 2010. "Numerical simulation of vortex shedding from an inclined flat plane." *Eng. Appl. Comp. Fluid Mech.* 4 (4): 569–579. https://doi.org/10.1080/19942060.2010.11015342.

Levi, E. 1983. "A universal Strouhal law." *J. Eng. Mech.* 109 (3): 718–727. https://doi.org/10.1061/(ASCE)0733-9399(1983)109:3(718).

Lienhard, J. H. 1966. *Synopsis of lift, drag, and vortex frequency data for rigid circular cylinders*. Pullman, WA: Washington State Univ.

McGregor, D. M. 1957. *An experimental investigation of the oscillating pressures on a circular cylinder in a fluid stream*. North York, ON, Canada: Univ. of Toronto Institute for Aerospace Studies.

MnDOT (Minnesota DOT). 2014. "Concept of operations prepared for Minnesota department of transportation (MnDOT) for rural intersection conflict warning systems II deployment." Accessed August 23, 2018. https://www.dot.state.mn.us/its/projects/2011-2015/rural-intersect-conflict-warn-system/documents/ricwsIIconops.pdf.

MnDOT (Minnesota DOT). 2015. "Traffic engineering: Rural intersection conflict warning system (RICWS)." Accessed December 1, 2018. http://www.dot.state.mn.us/trafficeng/signals/conflictwarning.html.

MnDOT (Minnesota DOT). 2016. *Improved structural design for rural intersection conflict warning signs (RICWS)*. St. Paul, MN: MnDOT.

Munson, B. R., A. P. Rothmayer, T. H. Okiishi, and W. W. Huebsch. 2012. *Fundamentals of fluid mechanics*, 7th ed. Hoboken, NJ: Wiley.

Musa, M., C. Hill, F. Sotiropoulos, and M. Guala. 2018. "Performance and resilience of hydrokinetic turbine arrays under large migrating fluvial bed forms." *Nat. Energy* 3 (10): 839–846. https://doi.org/10.1038/s41560-018-0218-9.

Norberg, C. 2001. "Flow around a circular cylinder: Aspects of fluctuating lift." *J. Fluids Struct.* 15 (3–4): 459–469. https://doi.org/10.1006/jfls.2000.0367.

Ortiz, X., D. Rival, and D. Wood. 2015. "Forces and moments on flat plates of small aspect ratio with application to PV wind loads and small wind turbine blades." *Energies* 8 (4): 2438–2453. https://doi.org/10.3390/en8042438.

Rai, M. M. 2013. "Flow physics in the turbulent near wake of a flat plane." *J. Fluid Mech.* 724 (Jun): 704–733. https://doi.org/10.1017/jfm.2013.185.

Raupach, M. R., R. A. Antonia, and S. Rajagopalan. 1991. "Rough-wall turbulent boundary layers." *Appl. Mech. Rev.* 44 (1): 1–25. https://doi.org/10.1115/1.3119492.

Roshko, A. 1954. *On the development of turbulent wakes from vortex streets*. Cleveland: National Advisory Committee for Aeronautics.

Sherman, R. J., and R. J. Connor. 2019. "Development of a fatigue design load for high-mast lighting towers." *J. Struct. Eng.* 145 (1): 04018228. https://doi.org/10.1061/(ASCE)ST.1943-541X.0002236.

Simiu, E., and D. H. Yeo. 2019. *Wind effects on structures: Modern structural design for wind*. 4th ed. Hoboken, NJ: Wiley.

Solari, G. 2017. "Gust buffeting of slender structures and structural elements: Simplified formulas for design calculations and code provisions." *J. Struct. Eng.* 144 (2): 04017185. https://doi.org/10.1061/(ASCE)ST.1943-541X.0001949.

Sun, Y., Y. Wu, Y. Qiu, and Y. Tamura. 2014. "Effects of free-stream turbulence and Reynolds number on the aerodynamic characteristics of a semi cylindrical roof." *J. Struct. Eng.* 141 (9): 04014230. https://doi.org/10.1061/(ASCE)ST.1943-541X.0001209.

Surry, D. 1972. "Some effects of intense turbulence on the aerodynamics of a circular cylinder at subcritical Reynolds number." *J. Fluid Mech.* 52 (3): 543–563. https://doi.org/10.1017/S0022112072001582.

Welch, P. D. 1967. "The use of fast Fourier transform for the estimation of power spectra: A method based on time averaging over short, modified period grams." *IEEE Trans. Audio Electroacoust.* 15 (2): 70–73. https://doi.org/10.1109/TAU.1967.1161901.

Williamson, C. H. K., and R. Govardhan. 2004. "Vortex-induced vibrations." *Annu. Rev. Fluid Mech.* 36 (Jan): 413–455. https://doi.org/10.1146/annurev.fluid.36.050802.122128.

Wu, T., and A. Kareem. 2013. "Vortex-induced vibration of bridge decks: Volterra series-based model." *J. Eng. Mech.* 139 (12): 1831–1843. https://doi.org/10.1061/(ASCE)EM.1943-7889.0000628.

Yang, D., B. Pettersen, H. I. Andersson, and V. D. Narasimhamurthy. 2012. "Vortex shedding in flow past an inclined flat plate at high incidence." *Phys. Fluids* 24 (8): 084103. https://doi.org/10.1063/1.4744982.

Zhu, Q., S. K. F. Stoter, M. Heisel, C. E. French, M. Guala, L. E. Linderman, and D. Schillinger. 2020. "Reducing wind-induced vibrations of road sign structures through aerodynamic modifications: A computational pilot study for a practical example." *J. Wind Eng. Ind. Aerodyn.* 199 (Apr): 104132. https://doi.org/10.1016/j.jweia.2020.104132.